Thermal conductivity and Lorenz ratio of metals at intermediate temperatures with mode-level first-principles analysis

Shouhang Li,[1] Zhen Tong,[1,2] Xinyu Zhang,[1] and Hua Bao[1,*]

[1]*University of Michigan-Shanghai Jiao Tong University Joint Institute, Shanghai Jiao Tong University, Shanghai 200240, People's Republic of China*

[2]*Shenzhen JL Computational Science and Applied Research Institute, Shenzhen 518109, People's Republic of China*

(Received 19 April 2020; revised 28 August 2020; accepted 21 October 2020; published 10 November 2020)

The electrical and thermal transport properties of metals become complicated in the intermediate and low temperature range ($0.1\Theta_D$–Θ_D, with Θ_D being the Debye temperature) due to electron-phonon inelastic scattering. For the Wiedemann-Franz law, a notable feature is that the Lorenz ratio significantly deviates from the Sommerfeld value. Although qualitatively theoretical understanding has been developed for decades, a mode-level first-principles analysis is still lacking in this temperature range and a better understanding of inelastic scattering and thermal transport mechanisms is desirable. In this work, we take aluminum and copper as examples. We find that two factors are essential to correctly predict the thermal conductivity and Lorenz ratio in the intermediate temperature range. First, the momentum relaxation time should be used for electrical conductivity calculations, while the energy relaxation time should be used for electronic thermal conductivity calculations. Second, proper choice of broadening parameter and fine sampling in the Brillouin zone is vital. Using the mode-level description of inelastic electron-phonon scattering at intermediate temperatures, the correct Lorenz ratio can be obtained within the present scheme, while using only the energy or momentum relaxation time cannot capture the correct trend of Lorenz ratio. The calculation scheme can be expanded to other metallic systems and is valuable for a better understanding of the transport properties of metals.

DOI: 10.1103/PhysRevB.102.174306

I. INTRODUCTION

Heat conduction in metals involves complicated electron and phonon transport and scattering processes, which has historically been a research focus in solid-state physics [1,2]. The Wiedemann-Franz law states that the ratio of electronic thermal conductivity (κ_{el}) to electrical conductivity (σ) is proportional to the absolute temperature T [3], and plays a vital role in evaluating the electronic thermal conductivity of metals. The proportionality constant (also known as the Lorenz ratio) is often taken as the Sommerfeld value, $L_0 = 2.44 \times 10^{-8}\ \mathrm{W\,\Omega/K^2}$. It has been well recognized that the Lorenz ratio is generally similar to the Sommerfeld value at low- or high-temperature ranges [4], in which the elastic electron-impurity scattering or nearly elastic electron-phonon scattering prevails. However, at the intermediate temperature range ($0.1\Theta_D$–Θ_D, with Θ_D being the Debye temperature) where inelastic electron-phonon scattering dominates, the Lorenz ratio can significantly deviate from the Sommerfeld value and the mechanism is worth exploring further [5].

Although experimental measurements of electrical and thermal conductivity are available for typical elemental metals at the intermediate temperature range [6], correctly obtaining electronic components of thermal conductivity is still challenging. In most experiments, the phonon thermal conductivity is simply neglected when calculating the Lorenz ratio [7]. In order to explicitly obtain electron and phonon contributions to thermal conductivity, one either needs to apply large magnetic fields to suppress electron transport [8,9], or use the complicated alloying method to extrapolate a series of samples with different solute concentrations [10]. Due to these difficulties, the experimental data are only available for a handful of simple metals [8,10,11]. On the other hand, to understand the underlining physics, the Bloch-Grüneisen (BG) model [5,12,13] developed in the 1930s is still widely used to explain the deviation of Lorenz ratio in the intermediate temperature range [8,14]. The variation with temperature for transport coefficients and Lorenz ratio can be partially captured by the BG model [5]. Nevertheless, the BG model is based on the assumptions of free electrons, the Debye phonon spectrum, and that electrons only scatter when interacting with longitudinal-acoustic phonons. Also, the inelastic electron-phonon scattering is treated with the ideal spherical Fermi-surface assumption [5]. Therefore, it is difficult to obtain the thermal conductivity and Lorenz ratio for metals at intermediate temperatures in a quantitative manner.

Recent advances in first-principles calculations allow researchers to quantitatively determine the transport coefficients of metals. Early calculations adopted constant electron relaxation time approximation combing first-principles electron band structure [15], which can introduce large deviations even in simple elemental metals [16,17]. Moreover, due to the assumption of constant relaxation time, the Wiedemann-Franz law must be valid for free-electron metals across the

*Author to whom correspondence should be addressed: hua.bao@sjtu.edu.cn

whole temperature range [5]. Allen's model, which is the lowest order variational approximation of the solution to the electron Boltzmann transport equation (BTE) [18], allows us to obtain the transport coefficients in real metallic systems. Nevertheless, non-negligible deviations still exist in some elemental metals in this model [19,20]. Recently, the accurate mode-level calculation of electron-phonon scattering is enabled by employing the maximally localized Wannier function (MLWF) interpolation technique [21]. Using this approach, explicit electron-phonon scattering rates can be extracted and substituted into the electron BTE. Combining this with anharmonic lattice dynamics, the phonon and electron thermal conductivities can be calculated separately. This method has been successfully applied to element metals [22–24], intermetallics [25], doped semiconductors [26–28], and intrinsic semiconductor at high temperature [29]. All these calculations are conducted at temperatures similar to or higher than the Debye temperature. As a result, the predicted Lorenz ratios in metals are quite consistent with the Sommerfeld value [23,24]. The mechanism of inelastic electron-phonon scattering and its effect on electron transport in metals at intermediate temperatures has not yet been carefully explored.

In this work, the thermal transport properties and Lorenz ratio at intermediate temperatures (10–300 K) for metals are studied from first principles with a detailed analysis of inelastic electron-phonon scattering. Two representative metals, copper (Cu) and aluminum (Al), are considered. We first review the transport theory of the electron BTE and describe the necessity of using different relaxation times for the electrical transport and thermal transport. Next, convergence issues for the transport coefficients with respect to the broadening parameter and mesh size for Brillouin-zone integration are examined. We point out the importance of these parameters to the correct prediction of the transport coefficients. The electrical conductivity and electronic thermal conductivity are then presented and compared with existing models. The mechanism of inelastic scattering and its effect on transport coefficients and Lorenz ratios in the intermediate temperature range are also discussed.

II. THEORY AND METHODS

The calculation of electron transport properties can be performed under the framework of the electron BTE. With both the external electrical field and temperature gradient, the steady-state linearized electron BTE can be written as

$$\left(-\frac{\partial f^0_{n\mathbf{k}}}{\partial \varepsilon_{n\mathbf{k}}}\right)\mathbf{v}_{n\mathbf{k}}\cdot\left[e\mathbf{E}+\frac{\varepsilon_{n\mathbf{k}}-\varepsilon_F}{T}\nabla T\right]=\left(\frac{\partial f_{n\mathbf{k}}}{\partial t}\right)_{\text{coll}}, \quad (1)$$

where $f^0_{n\mathbf{k}}$ is the electron equilibrium distribution at the electron mode $n\mathbf{k}$ (n-band index, $\mathbf{k}$-wave vector), namely Fermi-Dirac distribution. e is the elementary charge, $\varepsilon_{n\mathbf{k}}$ is the electron energy, ε_F is the Fermi energy, $\mathbf{v}_{n\mathbf{k}}$ is the electron group velocity, and $\mathbf{E}$ is the electrical field (both the external electrical field and the term $\nabla\varepsilon_F/e$ induced by the temperature gradient are included). The two terms on the left-hand side denote the deviations of the distribution function from the equilibrium state generated by electrical field and temperature gradient, respectively. The right-hand side is the electron collision term, which draws the system into equilibrium. Under the relaxation time approximation, the collision term is usually simplified as

$$\left(\frac{\partial f_{n\mathbf{k}}}{\partial t}\right)_{\text{coll}}=-\frac{f_{n\mathbf{k}}-f^0_{n\mathbf{k}}}{\tau_{n\mathbf{k}}}=-\frac{\delta f_{n\mathbf{k}}}{\tau_{n\mathbf{k}}}, \quad (2)$$

where $\tau_{n\mathbf{k}}$ is the relaxation times and it quantifies how quickly the electron returns to equilibrium [5].

In most works [22,25,27], $\tau_{n\mathbf{k}}$ is regarded to be the same for both electrical transport and thermal transport processes. However, recent work [4] proposed that the relaxation times for charge transport and energy transport should be distinct from each other in order to accurately capture the transport properties and Lorenz ratio at intermediate temperatures. Therefore, the deviation of the electron distribution within the relaxation time approximation can be expressed as [4,5]

$$\delta f_{n\mathbf{k}}=\tau_{\sigma,n\mathbf{k}}(T)e\mathbf{v}_{n\mathbf{k}}\cdot\mathbf{E}\left(\frac{\partial f^0_{n\mathbf{k}}}{\partial \varepsilon_{n\mathbf{k}}}\right)+\tau_{\kappa,n\mathbf{k}}(T)\times\frac{\varepsilon_{n\mathbf{k}}-\varepsilon_F}{T}\mathbf{v}_{n\mathbf{k}}\cdot\nabla T\left(\frac{\partial f^0_{n\mathbf{k}}}{\partial \varepsilon_{n\mathbf{k}}}\right), \quad (3)$$

in which $\tau_{\sigma,n\mathbf{k}}$ is the electrical relaxation time (also called momentum relaxation time) and $\tau_{\kappa,n\mathbf{k}}$ is the thermal relaxation time (also called energy relaxation time). If we only consider the electron-phonon scattering process, the scattering rate corresponding to the energy relaxation time can be determined from an integration of all scattering processes for the electron at $\varepsilon_{n\mathbf{k}}$ and expressed as

$$\frac{1}{\tau_{\kappa,n\mathbf{k}}}=\frac{2\pi}{\hbar}\sum_{m\mathbf{k}+\mathbf{q}}|g_{mn,v}(\mathbf{k},\mathbf{q})|^2\times\begin{Bmatrix}\left[n^0_{\mathbf{q}v}(T)+f^0_{m\mathbf{k}+\mathbf{q}}(T)\right]\delta(\varepsilon_{n\mathbf{k}}-\varepsilon_{m\mathbf{k}+\mathbf{q}}+\hbar\omega_{\mathbf{q}v})\\+\left[n^0_{\mathbf{q}v}(T)+1-f^0_{m\mathbf{k}+\mathbf{q}}(T)\right]\delta(\varepsilon_{n\mathbf{k}}-\varepsilon_{m\mathbf{k}+\mathbf{q}}-\hbar\omega_{\mathbf{q}v})\end{Bmatrix}, \quad (4)$$

where $n^0_{\mathbf{q}v}$ is the equilibrium Bose-Einstein distribution related to phonon $\mathbf{q}v$. The first and second terms in the curly braces are related to the absorption process and emission process during electron-phonon coupling, respectively. The electron-phonon coupling matrix element [30] can be expressed as

$$g_{mn,v}(\mathbf{k},\mathbf{q})=(2\omega_{\mathbf{q}v})^{-1/2}\langle\psi_{m\mathbf{k}+\mathbf{q}}|\Delta V_{\mathbf{q}v}|\psi_{n\mathbf{k}}\rangle, \quad (5)$$

where $\omega_{\mathbf{q}v}$ is the phonon frequency. $\psi_{n\mathbf{k}}$ and $\psi_{m\mathbf{k}+\mathbf{q}}$ are the initial and final Bloch electron states of the scattering process, respectively. ΔV is the first-order derivative of the Kohn-Sham potential.

The scattering rate corresponding to the momentum relaxation time at $\varepsilon_{n\mathbf{k}}$ is given by

$$\frac{1}{\tau_{\sigma,n\mathbf{k}}}=\sum_{m\mathbf{k}+\mathbf{q}}\frac{1}{\tau_{\kappa,n\mathbf{k},m\mathbf{k}+\mathbf{q}}}(1-\cos\theta_{n\mathbf{k},m\mathbf{k}+\mathbf{q}}). \quad (6)$$

The two scattering rates in a scattering process differ by an efficiency factor $\alpha_{n\mathbf{k},m\mathbf{k}+\mathbf{q}}=(1-\cos\theta_{n\mathbf{k},m\mathbf{k}+\mathbf{q}})$, which is located in the range of 0–2. Here $\theta_{n\mathbf{k},m\mathbf{k}+\mathbf{q}}$ is the scattering angle between the electron states $n\mathbf{k}$ and $m\mathbf{k}+\mathbf{q}$. With the assumption of $\tau_{n\mathbf{k}}\mathbf{v}_{n\mathbf{k}}\approx\tau_{m\mathbf{k}+\mathbf{q}}\mathbf{v}_{m\mathbf{k}+\mathbf{q}}$ [31], we have

$$\cos\theta_{n\mathbf{k},m\mathbf{k}+\mathbf{q}}=\frac{\mathbf{v}_{m\mathbf{k}+\mathbf{q}}\cdot\mathbf{v}_{n\mathbf{k}}}{|\mathbf{v}_{m\mathbf{k}+\mathbf{q}}||\mathbf{v}_{n\mathbf{k}}|}. \quad (7)$$

The efficiency factor arises from the fact that the scattering of electrical current is efficient only when the direction of electron motion is changed. However, the energy exchange occurs in any scattering process and thus the scattering efficiency of the heat current is always effective. Such a physical picture has been described in standard textbooks [5,32,33]. The relaxation times in Eqs. (4) and (6) are equivalent to the transport relaxation times mentioned in other places [34–36], shown in Appendix A. Note that in several works, either $\tau_{\sigma,n\mathbf{k}}$ [22,27] or $\tau_{\kappa,n\mathbf{k}}$ [23,37] is used to predict both electrical conductivity and electronic thermal conductivity. This may not cause much error at the high-temperature range since the large-angle scatterings dominate the scattering processes. However, as will be shown later, at lower temperatures, the correct relaxation times must be employed in order to obtain accurate transport properties and Lorenz ratios.

The electrical current ($\mathbf{J}$) and heat current ($\mathbf{Q}$) can be expressed as [5]

$$\begin{aligned}\mathbf{J} &= \sum_{n\mathbf{k}} e\mathbf{v}_{n\mathbf{k}} f_{n\mathbf{k}} = \sum_{n\mathbf{k}} e\mathbf{v}_{n\mathbf{k}}\left(f^0_{n\mathbf{k}} + \delta f_{n\mathbf{k}}\right)\\ \mathbf{Q} &= \sum_{n\mathbf{k}} (\varepsilon_{n\mathbf{k}} - \varepsilon_F)\mathbf{v}_{n\mathbf{k}} f_{n\mathbf{k}} = \sum_{n\mathbf{k}} (\varepsilon_{n\mathbf{k}} - \varepsilon_F)\mathbf{v}_{n\mathbf{k}}\left(f^0_{n\mathbf{k}} + \delta f_{n\mathbf{k}}\right).\end{aligned} \tag{8}$$

Insert Eq. (3) into Eq. (8) and we get

$$\begin{aligned}\mathbf{J} &= L_{EE}\mathbf{E} + L_{ET}\nabla T\\ \mathbf{Q} &= L_{TE}\mathbf{E} + L_{TT}\nabla T,\end{aligned} \tag{9}$$

with the coefficients given by

$$\begin{aligned}L_{EE} &= -\frac{e^2}{N_{\mathbf{k}}V}\sum_{m\mathbf{k}} v_{m\mathbf{k},\alpha} v_{m\mathbf{k},\beta}\tau_{\sigma,m\mathbf{k}}(\varepsilon_F, T)\\ &\quad\times \frac{\partial f^0(\varepsilon_{m\mathbf{k}}, \varepsilon_F, T)}{\partial \varepsilon_{m\mathbf{k}}}\\ L_{ET} &= -\frac{e}{N_{\mathbf{k}}VT}\sum_{m\mathbf{k}} v_{m\mathbf{k},\alpha} v_{m\mathbf{k},\beta}\tau_{\kappa,m\mathbf{k}}(\varepsilon_F, T)(\varepsilon_{m\mathbf{k}} - \varepsilon_F)\\ &\quad\times \frac{\partial f^0(\varepsilon_{m\mathbf{k}}, \varepsilon_F, T)}{\partial \varepsilon_{m\mathbf{k}}}\\ L_{TE} &= -\frac{e}{N_{\mathbf{k}}V}\sum_{m\mathbf{k}} v_{m\mathbf{k},\alpha} v_{m\mathbf{k},\beta}\tau_{\sigma,m\mathbf{k}}(\varepsilon_F, T)(\varepsilon_{m\mathbf{k}} - \varepsilon_F)\\ &\quad\times \frac{\partial f^0(\varepsilon_{m\mathbf{k}}, \varepsilon_F, T)}{\partial \varepsilon_{m\mathbf{k}}}\\ L_{TT} &= \frac{1}{N_{\mathbf{k}}V}\sum_{m\mathbf{k}} \frac{(\varepsilon_{m\mathbf{k}} - \varepsilon_F)^2}{T} v_{m\mathbf{k},\alpha} v_{m\mathbf{k},\beta}\tau_{\kappa,m\mathbf{k}}(\varepsilon_F, T)\\ &\quad\times \frac{\partial f^0(\varepsilon_{m\mathbf{k}}, \varepsilon_F, T)}{\partial \varepsilon_{m\mathbf{k}}}.\end{aligned} \tag{10}$$

α and β are Cartesian coordinate components. $N_{\mathbf{k}}$ is the total number of $\mathbf{k}$ points in the first Brillouin zone. V is the volume of the unit cell.

From Eq. (9), the electrical and thermal conductivity have the following expression using the definitions of the two transport coefficients,

$$\begin{aligned}\sigma &= L_{EE}\\ \kappa_{\text{el}} &= -\left(L_{TT} - \tfrac{L_{TE}L_{ET}}{L_{EE}}\right).\end{aligned} \tag{11}$$

The term $\frac{L_{TE}L_{ET}}{L_{EE}}$ in the expression of electronic thermal conductivity is very small in metals and is usually ignored. Therefore, only energy relaxation time τ_κ is contained in electronic thermal conductivity in our later calculations. Note that for L_{EE}, the momentum relaxation time is adopted, while for L_{TT}, the energy relaxation time is used.

In the subsequent discussions, we consider two common metals, copper (Cu) and aluminum (Al), as examples. The first-principles calculations are carried out with Quantum ESPRESSO [38]. A Perdew-Burke-Ernzerhof (PBE) form [39] of the exchange-correlation functional is employed. The cutoff energy of the plane wave is set to be 180 Ry for Cu and 100 Ry for Al to ensure convergence, and the convergence threshold of electron energy is set to be 10^{-10} Ry for the self-consistent field calculation.

The lattice vectors and atomic positions are fully relaxed based on the Broyden-Fretcher-Goldfarb-Shanno (BFGS) optimization method [40–43]. The optimized lattice constants come out to be 3.669 and 4.043 Å (experimental values are 3.615 and 4.050 Å) [44] for Cu and Al with face-centered-cubic (fcc) lattice, respectively. For the electronic properties calculations, the two categories of electron-phonon scattering rates are calculated using our in-house modified electron-phonon Wannier (EPW) package [30]. The phonon spectrums are obtained on $6 \times 6 \times 6$ $\mathbf{q}$-point mesh using density functional perturbation theory (DFPT) [45] and the spectrums match experimental data well, as shown in Sec. S1 of the Supplemental Material [46] (see, also, Refs. [47,48] therein). The electron-phonon coupling matrix elements are first calculated on the coarse grids of $12 \times 12 \times 12$ $\mathbf{k}$ point and $6 \times 6 \times 6$ $\mathbf{q}$ point, and are then interpolated to the sufficiently dense $\mathbf{k}$-point and $\mathbf{q}$-point meshes to ensure the convergence of electrical transport coefficients in the whole temperature range. The electron band structures calculated under the Wannier scheme match density function theory (DFT) band structures quite well, as shown in Sec. S1 of the Supplemental Material [46].

To calculate the phonon thermal conductivity component, we employed the widely used anharmonic lattice dynamics scheme to calculate the phonon-phonon scattering process [49]. The harmonic force constant is obtained employing the DFPT [45] under a $6 \times 6 \times 6$ $\mathbf{q}$-point mesh. The cubic force constant is extracted with the THIRDORDER.PY package [49]. A supercell of $4 \times 4 \times 4$ is used and the third nearest neighbor is considered for the cubic force-constant calculation. A $3 \times 3 \times 3$ $\mathbf{k}$-point mesh is used and the convergence is ensured. Note that in metals, the limitations of phonon-electron scattering to phonon thermal conductivity must also be considered. The calculation method of phonon-electron scattering and phonon thermal conductivity has been described in our previous works [23] and thus not repeated here.

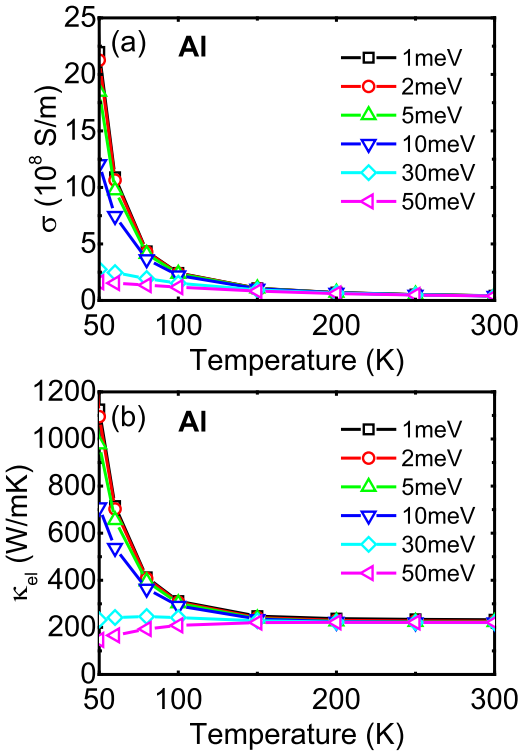

FIG. 1. Variations of (a) electrical conductivity and (b) electronic thermal conductivity of Al in the temperature range of 50–300 K with broadening parameters 1, 2, 5, 10, 30, and 50 meV. The **q**- and **k**-point meshes are set as 60 × 60 × 60 and 200 × 200 × 200, respectively.

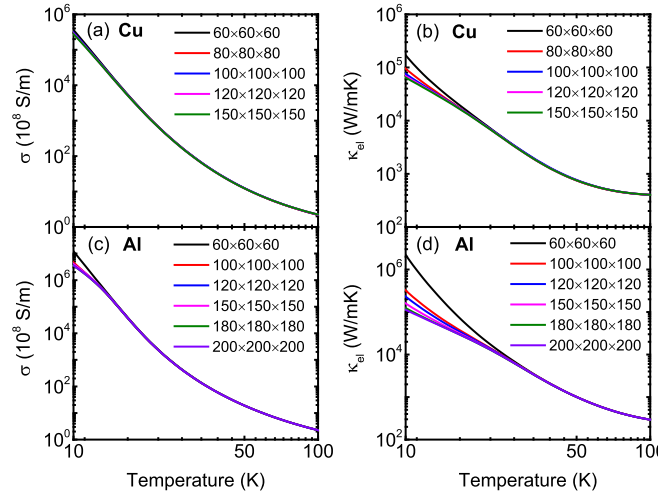

FIG. 2. Calculated electrical conductivity for (a) Cu and (c) Al with respect to the **q**-point meshes in the temperature range of 10–100 K. Calculated electronic thermal conductivity for (b) Cu and (d) Al with respect to the **q**-point meshes in the temperature range of 10–100 K. The **k**-point mesh size is kept as 200 × 200 × 200 in all the calculations.

III. RESULTS AND DISCUSSIONS

A. Convergence study

In order to obtain the correct relaxation times in Eqs. (4) and (6) numerically, Brillouin-zone integration needs to be performed. Unlike in the calculations at high temperatures, the electron-phonon scattering at intermediate temperature is weak and very dense Brillouin-zone sampling must be performed in order to obtain the converged electron relaxation times [50]. The approximation form employed for the δ function in Eq. (4) is also a curial issue in the convergence of electron scattering rates. In this work, we follow the method described in Ref. [30] and adopt the Gaussian broadening scheme as $\delta(x) = \lim_{\eta\to 0}\frac{1}{\sqrt{\pi}}\frac{1}{\eta}e^{-(x/\eta)^2}$. The choice of the broadening parameter η must be balanced with the density of **q**- and **k**-point sampling. Usually, a small enough η compatible with **q**- and **k**-point mesh is used. As will be shown below, inappropriate usage of the Gaussian broadening parameter can yield unphysical results.

We predict the electrical conductivity and electronic thermal conductivity with six different η values, 1, 2, 5, 10, 30, and 50 meV, in Al. The **q**- and **k**-point meshes are set as relatively dense values, 60 × 60 × 60 and 200 × 200 × 200, respectively. As it is shown in Fig. 1, there is not much difference in both electrical and thermal conductivity with different η when the temperature is larger than 200 K. However, significant deviations appear in both electrical and thermal conductivity when the temperature is below 150 K. When the broadening parameter is set to be 30 or 50 meV, the electronic thermal conductivity displays an increasing trend in temperature, which contradicts experimental observations [6]. Note that such an unphysical phenomenon was observed in previous calculations [22] and it is expected to be related to the improper use of η. As it is shown in Sec. S2 of the Supplemental Material [46], η should be reduced to 10 meV to ensure the convergence of the energy scattering rate of Al at 100 K. The larger η would significantly overestimate the scattering rate. However, a large value of $\eta = 30$ meV can also ensure the convergence of scattering rates at 300 K, which is the case in Ref. [22]. η is set as 30 meV in the whole temperature range in Ref. [22]. As thus, we expect the electronic thermal conductivity of Al to be underestimated below 300 K in Ref. [22], resulting in the unphysical behavior. Therefore, to accurately obtain the converged electron-scattering rates, smaller η should be used as the smearing of the Fermi-Dirac distribution will be smaller with decreasing temperature. The value of k_BT (k_B is the Boltzmann constant) for η works well for the cases in this work.

Because small Gaussian broadening parameters are employed at low temperatures, an ultradense **q**-point mesh and **k**-point mesh should be used to ensure the convergence of electron-scattering rates. Here we present the convergence test using different **q**-point meshes for both electrical conductivity and electronic thermal conductivity of Cu, as shown in Fig. 2. An ultradense **k**-point mesh of 200 × 200 × 200 is fixed for all cases, as it is dense enough to capture the variation in scattering rates near the Fermi surface. Both electrical conductivity and electronic thermal conductivity get converged easier as the temperature is larger than 40 K, where we find that 60 × 60 × 60 **q**-point mesh is enough to achieve convergence. In comparison, for temperatures below 40 K, an extremely dense **q**-point mesh of 150 × 150 × 150 (200 × 200 × 200) is sufficiently large to ensure the convergence of electrical

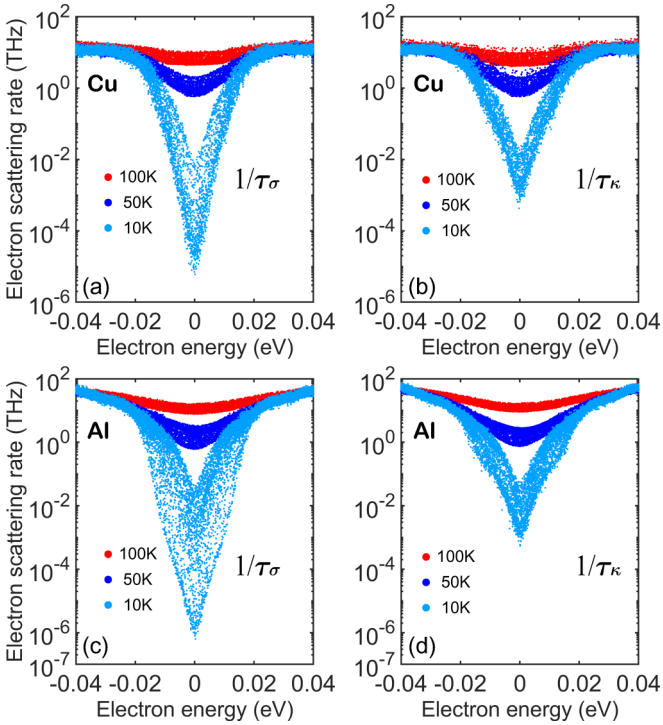

FIG. 3. The electron scattering rates ($1/\tau_\sigma$) corresponding to momentum relaxation times with different temperatures for (a) Cu and (c) Al. The electron scattering rates ($1/\tau_\kappa$) corresponding to energy relaxation times with different temperatures for (b) Cu and (d) Al. The electron energy is normalized to Fermi energy (ε_F).

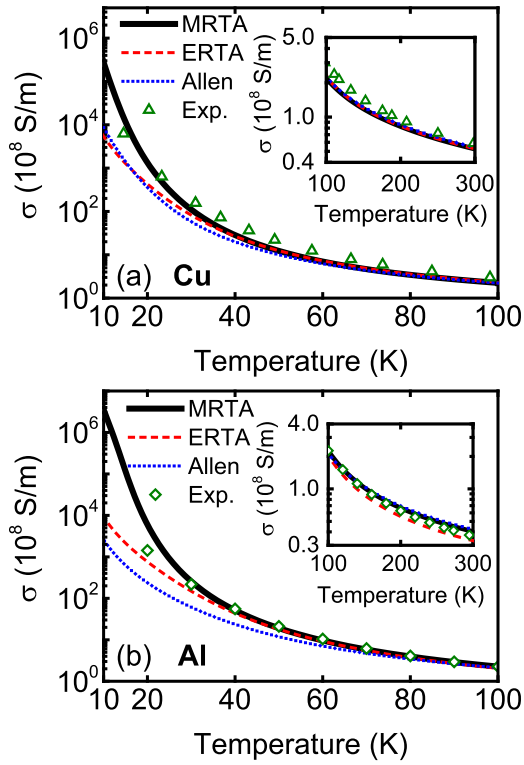

FIG. 4. The electrical conductivity for (a) Cu and (b) Al calculated with MRTA (black solid lines), ERTA (red dash lines), and Allen's model (blue dot lines). The experimental data are taken from Ref. [52]. The insets of (a) and (b) are the electrical conductivity in the temperature range of 100–300 K. The ideal experimental data is obtained by subtracting the residual resistance from the total resistance. The results predicted by the correct model are in bold lines.

conductivity and thermal conductivity for Cu (Al). Small **q**-point meshes can result in an overestimation of the two transport coefficients due to the insufficient scattering phase space accessible for electron modes. Note that even denser **q**-point meshes are needed to ensure the convergence at lower temperatures. We do not consider the temperatures below 10 K due to the formidable computation cost. Therefore, we use $150 \times 150 \times 150$ **q**-point mesh for Cu and $200 \times 200 \times 200$ **q**-point mesh for Al in the subsequent calculations.

The converged electron-scattering rates corresponding to momentum and energy relaxation times at different temperatures for Cu and Al are shown in Fig. 3. The scattering rates increase significantly with temperature, which is mainly due to the increase of phonon distribution n^0. A drastic variation appears near the Fermi surface. There is a sharp decrease of around five orders of magnitude for $1/\tau_\sigma$ and around three orders of magnitude for $1/\tau_\kappa$ as the temperature goes from 100 K to 10 K for Cu. It clearly demonstrates that the constant electron relaxation time assumption [15] may give a large uncertainty for calculating the electrical transport properties and the mode-level calculation is necessary. The difference between $1/\tau_\sigma$ and $1/\tau_\kappa$ is small at 50 and 100 K for both Cu and Al. But the difference is large at 10 K, which is more than one order of magnitude in Cu. There are valleys near the Fermi energy as the temperature is less than 100 K. It originates from the suppression of long wave-vector phonon modes as the temperature decreases. A similar phenomenon is also observed in the calculation for Pb [50].

B. Electrical transport coefficients

The electrical conductivities for Cu and Al calculated using momentum relaxation time approximation (MRTA), energy relaxation time approximation (ERTA), and Allen's model [18,51] are shown in Fig. 4. The experimental data [52] are also presented for comparison. The electrical conductivities are found to decrease with the increase of temperature. This is related to the increase in electron-phonon scattering with temperature. Overall, the electrical conductivity predicted by MRTA is closer to the experimental data [52] in the whole temperature range. The ideal experimental electrical conductivity is obtained by subtracting the residual resistance from the total electrical resistance of the material. Here we only consider the electrical transport properties limited by phonons in the calculations. It should be noted that the electron-electron scattering can further impede electron transport if the temperatures are very low. As such, our predicted electrical conductivity should be larger than the intrinsic experimental data for temperatures below 15 K. The energy relaxation time approximation (ERTA) is also employed in electrical conductivity prediction in previous works [23,37,53]. We found that the electrical conductivity predicted by ERTA is very close to that evaluated by MRTA when the temperature is greater than 40 K for Cu. However, the difference becomes

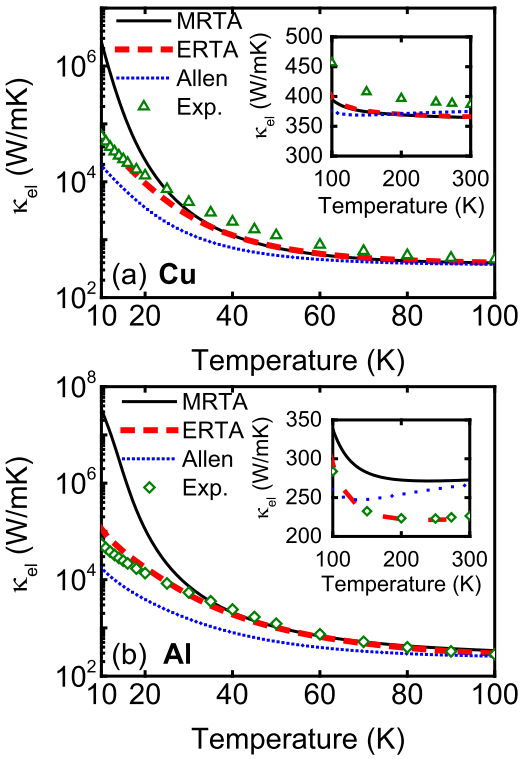

FIG. 5. The electronic thermal conductivity for (a) Cu and (b) Al calculated with MRTA (black solid lines), ERTA (red dash lines), and Allen's model (blue dot lines). The experimental data are taken from Ref. [6]. The insets of (a) and (b) are the electronic thermal conductivity in the temperature range of 100–300 K. The ideal experimental data are obtained by subtracting the residual thermal resistance from the total thermal resistance. The phonon thermal conductivity (obtained by first-principles calculation) is also subtracted from the experimental thermal conductivity. The results predicted by the correct model are in bold lines.

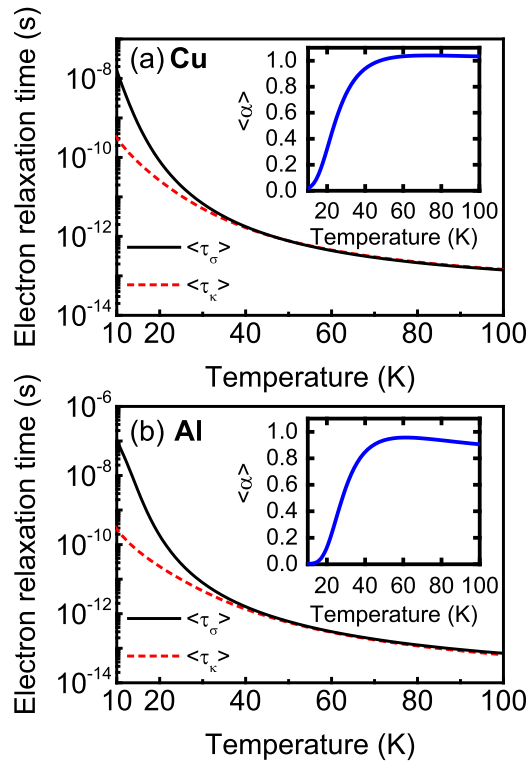

FIG. 6. The average momentum relaxation time $\langle\tau_\sigma\rangle$ and energy relaxation time $\langle\tau_\kappa\rangle$ with different temperatures for (a) Cu and (b) Al. The insets are the average efficiency factors $\langle\alpha\rangle$ for Cu and Al, respectively.

significant once the temperature gets below 40 K. This arises from the difference between the two relaxation times, as later shown in Fig. 6(a). The momentum relaxation time is larger than the energy relaxation time and ultimately results in the smaller electrical conductivity in ERTA. It should be noted that the difference between ERTA and MRTA is noticeable in Al even at temperatures of 100–300 K, which was also observed in the previous study [54]. These results demonstrate that ERTA is inappropriate in the prediction of electrical conductivity for Al even at room temperature. Allen's model is also widely used to predict electrical transport coefficients [19,20,55,56]. Details of Allen's model can be found in Appendix B. The predicted electrical conductivities using Allen's model are shown as the blue dotted lines in Fig. 4. Allen's model matches the MRTA model well in the temperature range of 100–300 K. However, it has a significant deviation from MRTA as the temperature is below 60 K for Cu and 80 K for Al.

The electronic thermal conductivity of Cu and Al is shown in Fig. 5. It first decreases dramatically with temperatures below 40 K, and then tends to a constant value as the temperature increases. Electronic thermal conductivity is related to electronic heat capacity and energy relaxation time. The heat capacity linearly increases with temperature. The energy relaxation time decreases dramatically with temperature in the low-temperature range, as it is shown in Fig. 6. Hence, the electronic thermal conductivity decreases quickly with temperature. At higher temperatures, the energy relaxation time is almost inversely proportional to the temperature due to the increase of phonon distribution n^0, resulting in the less temperature-dependent electronic thermal conductivity. The electronic thermal conductivity predicted by ERTA matches the experimental data [6] well within the entire temperature range. For Cu, the difference between ERTA and MRTA is less than 5% when the temperatures are larger than 40 K, while the difference is significant in the whole temperature range for Al. Specifically, the difference is ∼22% at 300 K for Al. This can be similarly interpreted as we have done in electrical conductivity.

The electronic thermal conductivities predicted by Allen's model are also presented. Allen's model can capture the variation features of electronic thermal conductivity for both Cu and Al. However, it has significant deviations from ERTA within the entire temperature range. It should be noted that the electronic thermal conductivity predicted by Allen's model holds a slightly increasing trend as the temperature is larger than 150 K, shown in the insets of Fig. 5. We expect such a phenomenon to be induced by the lowest-order approximation in Allen's model [18], as higher-order terms can also have a contribution to the thermal resistance. Moreover, Allen's model cannot consider the anisotropy (variation with **k** in the Fermi surface) and Fermi smearing effects [18,51]. It takes

the average scattering rate and velocity around the Fermi energy. Actually, the electron modes with energy in the range of $\varepsilon_F \pm dE$ contribute to the electronic thermal conductivity and the electron scattering rate cannot be approximated as a constant at the Fermi surface, as shown in Fig. 3. The variation of electrical and thermal conductivity at 100 K with a width of the Fermi window (dE) is shown in Sec. S3 of the Supplemental Material [46]. To ensure the convergence, the Fermi window width is set as 0.1 eV for temperatures smaller than 100 K, and it is set as 1.0 eV for temperatures within 100–300 K.

We further perform the calculations on electrical transport properties of superconductivity metals niobium (Nb) and tantalum (Ta), shown in Secs. S4 and S5 of the Supplemental Material [46]. Similar to Cu and Al here, the ERTA would underestimate the electrical conductivity and the MRTA would overestimate the electronic thermal conductivity at low temperatures.

C. Electron relaxation times

To further analyze the differences in the results predicted by MRTA and ERTA, the weighted averages of momentum relaxation time and energy relaxation time are given by [57]

$$\langle \tau_\sigma \rangle = \frac{\sum_{\mathbf{k}m} \frac{\partial f^0_{\mathbf{k}m}}{\partial \varepsilon_{\mathbf{k}m}} |v_{\mathbf{k}m}|^2 \tau_{\sigma,\mathbf{k}m}}{\sum_{\mathbf{k}m} \frac{\partial f^0_{\mathbf{k}m}}{\partial \varepsilon_{\mathbf{k}m}} |v_{\mathbf{k}m}|^2}$$
$$\langle \tau_\kappa \rangle = \frac{\sum_{\mathbf{k}m} \frac{\partial f^0_{\mathbf{k}m}}{\partial \varepsilon_{\mathbf{k}m}} |v_{\mathbf{k}m}|^2 \tau_{\kappa,\mathbf{k}m}}{\sum_{\mathbf{k}m} \frac{\partial f^0_{\mathbf{k}m}}{\partial \varepsilon_{\mathbf{k}m}} |v_{\mathbf{k}m}|^2} \quad (12)$$

with $|v_{\mathbf{k}m}|^2 = (v^x_{\mathbf{k}m})^2 + (v^y_{\mathbf{k}m})^2 + (v^z_{\mathbf{k}m})^2$.

The momentum and energy relaxation times both show a similar temperature dependence for Cu and Al, as shown in Fig. 6. They show a rapid decline when the temperature is less than 40 K and then the decreasing trend slows down in the higher temperature range. The magnitude of momentum relaxation time is significantly larger than that of energy relaxation time for Cu and Al at low temperatures. This indicates that the efficiency factor has a significant effect on electron scattering in this temperature range. To quantify the effects of the efficiency factor, the average efficiency factor $\langle \alpha \rangle$ is given by

$$\langle \alpha \rangle = (1/\langle \tau_\sigma \rangle)/(1/\langle \tau_\kappa \rangle). \quad (13)$$

As can be seen in the inset of Fig. 6(a), the average efficiency factor increases with temperatures below 40 K for Cu and converges to ~1.0 in the higher temperature range. It should be noted that the efficiency factor is close to 1 in the vicinity of 50 K and there exists a slight fall in Al at higher temperatures, which is different from the variation trend of Cu.

D. Lorenz ratio

The temperature-dependent Lorenz ratios of different models are presented in Fig. 7. According to the kinetic theory of electrons [5], the Lorenz ratio for metals should be the Sommerfeld value, as $L_0 = \pi^2 k_B^2/(3e^2) = 2.44 \times 10^{-8}\ \mathrm{W\,\Omega/K^2}$. This is based on the constant relaxation time assumption for free-electron metals. However, based on our present work

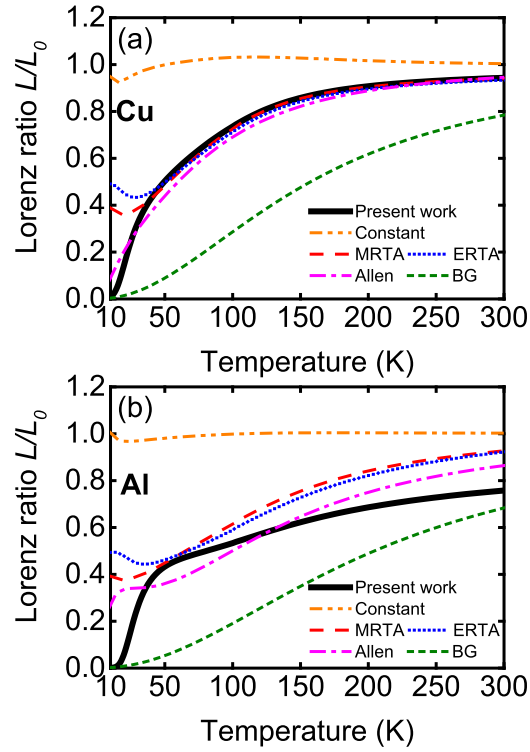

FIG. 7. The temperature dependent Lorenz ratio predicted in the present work, by constant relaxation time (Constant), MRTA, ERTA, Allen's model (Allen) and the BG model for (a) Cu and (b) Al. The Lorenz ratio is normalized by the Sommerfeld value, as $L_0 = 2.44 \times 10^{-8}\ \mathrm{W\,\Omega/K^2}$.

(momentum relaxation time for electrical conductivity and energy relaxation time for electronic thermal conductivity), the Lorenz ratio is no longer a constant at intermediate temperatures. It approaches zero at low temperatures and goes toward L_0 with temperature increasing. Our predicted Lorenz ratio is consistent with the existing theory [4], which states that the Lorenz ratio should be very small in the low-temperature range and increase with temperature if only electron-phonon scattering was considered. The Lorenz ratio predicted by constant relaxation time is almost temperature independent and very close to the Sommerfeld value. The Lorenz ratios predicted by ERTA and MRTA also have large variations with temperature, which indicates that the variation is induced by the mode-dependent electron relaxation time.

The Lorenz ratios predicted by ERTA and MRTA have large deviations from the present work in the lower temperature range, which further confirms that only momentum relaxation time is used for electrical conductivity and energy relaxation time for thermal conductivity can capture the correct Lorenz ratio. However, these two models predict similar Lorenz ratios as in the present work when the temperature is higher than 40 K for Cu. This is because the two relaxation times do not differ much in that temperature region. For Al, the Lorenz ratios predicted by ERTA and MRTA approach that of the present work only in the vicinity of 50 K and significant deviations exist in other temperature ranges. The average momentum relaxation time and average energy relaxation time are close to each other at ~50 K. Therefore,

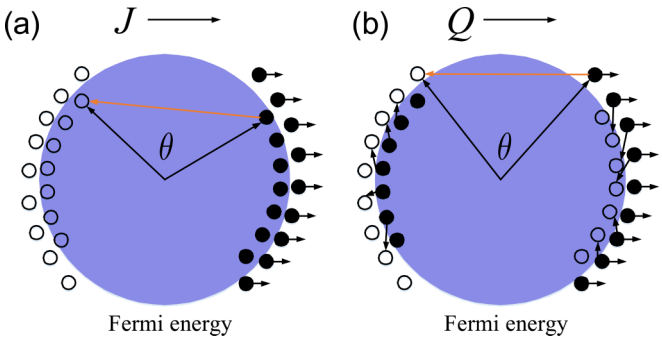

FIG. 8. Schematic representation of electron scattering in (a) an electric field and (b) under a temperature gradient. The electrons close to the Fermi surface are driven by the external perturbations. As for the external electrical field, the electrons can only return to equilibrium through large-angle scatterings (horizontal processes), as illustrated by the orange arrow in (a). As for the external temperature gradient, the electrons can return to equilibrium through both large-angle scatterings [orange arrow in (b)] and small-angle scatterings (vertical processes), as illustrated by the small black arrows in (b). The filled small spheres are occupied electron states and the open small spheres are unoccupied electron states.

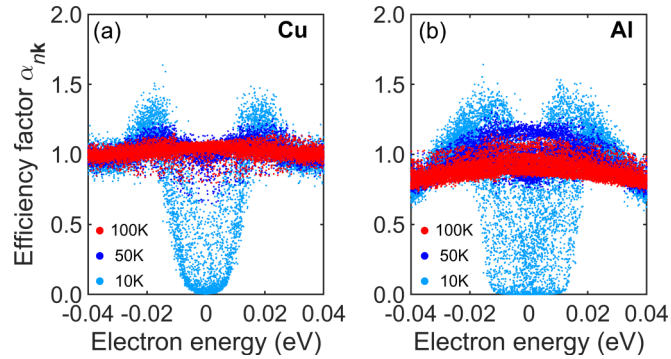

FIG. 9. The efficiency factor at electron mode n **k** with different temperatures for (a) Cu and (b) Al. The electron energy is normalized to Fermi energy (ε_F).

the further Lorenz ratio difference between the present work and single relaxation time models is induced by the large difference in the two relaxation times τ_σ and τ_κ.

The Lorenz ratios predicted by Allen's model and the BG model are also shown in Fig. 7. Allen's model replicates the Lorenz ratio of the present work in almost the entire temperature range in Cu, while deviations exist in Al. The BG model can be regarded as a special case of Allen's model [51]. The details about the BG model are presented in Appendix C. The Lorenz ratio predicted by the BG model holds the similar variation tendency with our present method, which is attributed to the two relaxation times being also employed in the BG model [5]. Also, the Lorenz ratio predicted by the BG model converges to 1 as the temperature is high. However, it does not match our first-principles calculation in a quantitative manner. This is attributed to the strong assumptions in the BG model.

E. Inelastic electron-phonon scattering

The anomalous behavior of the Lorenz ratio at low temperatures in Fig. 7 can be further attributed to the inelastic electron-phonon scattering, which induces the difference between momentum relaxation time and energy relaxation time. The electron-scattering processes for electrical current and heat current are different [5,33], as shown in Fig. 8. The electrons driven by the external electric field can only be scattered by the large-angle scattering (horizontal process) and return to equilibrium, which can change the direction of motion. In comparison, the electrons driven by the external temperature gradient can be effectively scattered by both the large-angle scattering and the small-angle scattering (vertical process). The type of large-angle scattering is sometimes also called quasielastic scattering, while the small-angle scattering is sometimes also called inelastic scattering. One should note there always exists energy transport in an electron-phonon scattering process. Strictly speaking, both large-angle scatterings and small-angle scatterings are inelastic.

At low temperatures, the electron scattering from long wave-vector phonons is largely suppressed and the short wave-vector phonons are the dominant scattering sources for electrons. Short wave-vector phonons cannot easily switch the direction of electron motion, but they do affect the energy transport of electrons by inelastic scattering. As a result, the momentum relaxation time is larger than the energy relaxation time. To further clarify this mechanism, the mode-level efficiency factor $\alpha_{n\mathbf{k}}$, as $(1/\tau_{\sigma,n\mathbf{k}})/(1/\tau_{\kappa,n\mathbf{k}})$, is presented in Fig. 9. The efficiency factor at 10 K for the electron modes close to the Fermi energy is significantly smaller than one for both Cu and Al, which indicates the significant inelastic scattering. There is almost no difference between 100 and 50 K for Cu and the value approaches 1, implying that the quasielastic scattering dominates. The efficiency factor of Al has a deviation from 1 at 100 K. Note that the value at 100 K is slightly smaller than that at 50 K. This is consistent with the decreasing trend of the average efficiency factor at higher temperatures in the inset of Fig. 6(b).

The Fermi surface with a superimposed efficiency factor $\alpha_{n\mathbf{k}}$ is shown in Fig. 10. The topological features of Cu and Al are completely different. The Fermi surface of Cu is close to spherical in shape while Al holds the irregular Fermi surface. There is only one sheet for Cu and two sheets for Al. The Fermi surface of Cu shows "neck," "belly," and "bulge" features in the regions marked by L, K, and X points, respectively [16]. However, the inner sheet of the Fermi surface of Al overall shows a "depression" trend toward the Brillouin-zone center. We can clearly see the anisotropy of the efficiency factor on the Fermi surface which is related to the topology of the Fermi surface. The blue ribbons on Fermi surfaces at 10 K in Fig. 10 for Cu and Al correspond to the small values in Fig. 9. The electron modes near the bulges hold the smallest efficiency factor at 50 and 100 K for Cu. The electron modes close to the Brillouin-zone boundary hold larger efficiency factors, and the depression regions of the inner sheet have smaller efficiency factors in Al. Most regions of the Fermi surface of Al hold smaller efficiency factors at 100 K compared to 50 K, which eventually results in the slightly smaller average efficiency factors at 100 K, as shown in the inset of Fig. 6(b).

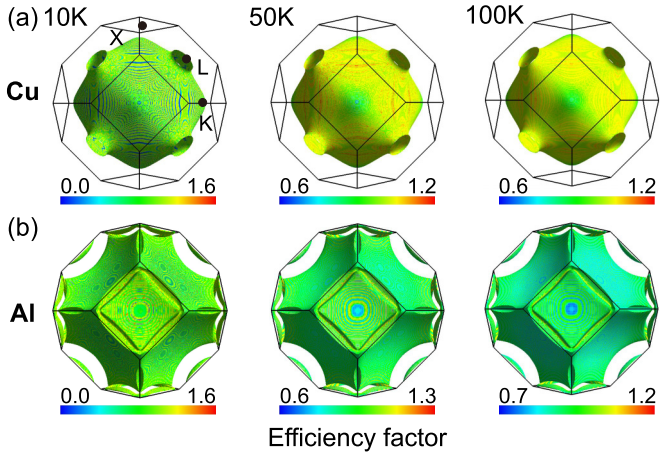

FIG. 10. Fermi surfaces showing the efficiency factor at electron mode $n\mathbf{k}$ at 10, 50, and 100 K for (a) Cu and (b) Al. There is only one sheet for the Fermi surface of Cu, while there are two sheets for the Fermi surface of Al. Note the different scales at different temperatures. *L*, *K*, and *X* are the three high-symmetry points of the Brillouin zone. The Fermi surfaces are plotted with the FermiSurfer package [58].

F. Phonon thermal conductivity

The phonon thermal conductivity ($\kappa_{\rm ph}$) for both Cu and Al at temperatures ranging from 10 to 300 K is shown in Fig. 11. Both phonon-phonon and phonon-electron scattering are included in the estimation of $\kappa_{\rm ph}$. As we can see, the phonon thermal conductivity first increases with temperature and then decreases with temperature. The increase at low temperatures is related to the increase of phonon heat capacity. Phonon-electron scattering is the main phonon-scattering source in this region and it is weakly dependent on the temperature [59]. It would have a significant effect on the phonon thermal conductivity as the temperature is smaller than 100 K, as shown in Appendix D. The decrease at higher temperatures is mainly attributed to the increase of anharmonic phonon-phonon scattering. Note that $\kappa_{\rm ph}$ occupies only a small proportion of the total thermal conductivity, as it is smaller than 5% in the entire temperature range. The Lorenz ratio will have a minor change if the total thermal conductivity is included in its estimation. In this work, the iterative calculation scheme [49] is employed in calculating intrinsic phonon thermal conductivity. This is important as the RTA calculation scheme would underestimate intrinsic phonon thermal conductivity at intermediate temperatures. We note that the phonon thermal conductivity of Cu at 300 K is smaller than the value reported in Ref. [23], which is attributed to the different pseudopotentials used for the DFT calculation. This issue has been discussed in Ref. [59].

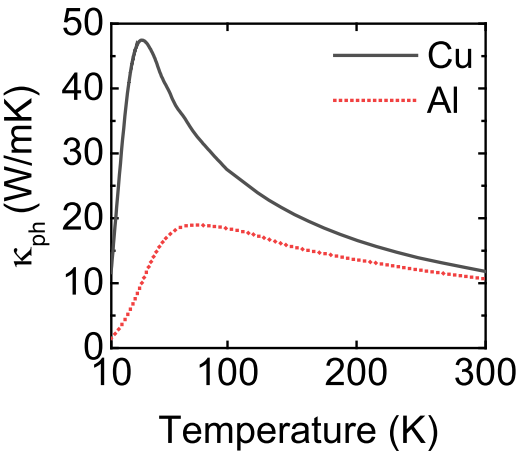

FIG. 11. The phonon thermal conductivity for Cu (solid line) and Al (dot line) in the temperature range of 10–300 K. Both phonon-phonon and phonon-electron scattering effects are included.

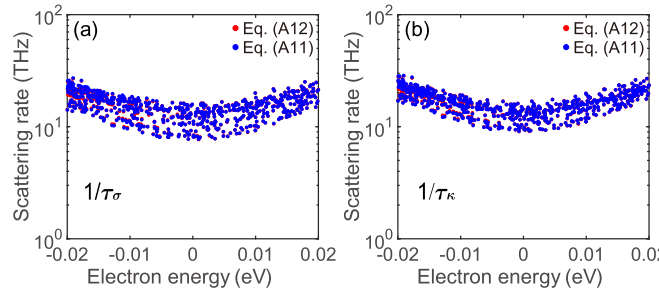

FIG. 12. The electron-scattering rates calculated using Eqs. (A11) and (A12) for (a) momentum scattering rate ($1/\tau_\sigma$) and (b) energy scattering rate ($1/\tau_\kappa$). The calculation is conducted on Al at 100 K with $80 \times 80 \times 80$ **q**-point mesh and $100 \times 100 \times 100$ **k**-point mesh. The electron energy is normalized to the Fermi energy (ε_F).

IV. CONCLUSIONS

In summary, we perform a rigorous first-principles study on the thermal conductivity and Lorenz ratio for Cu and Al in the temperature range of 10–300 K. The small broadening parameter, extremely dense **k**-point and **q**-point meshes, should be used in order to obtain the correct electrical transport coefficients at intermediate temperatures. It is shown that momentum relaxation time should be used for electrical conductivity and energy relaxation time for electronic thermal conductivity. Large deviations in Cu would occur at temperatures below 40 K and non-negligible deviations even at room temperature in Al if the electron relaxation times were misused. It is found that there is an intrinsic deviation of the Lorenz ratio from the Sommerfeld value as the temperature is smaller than 40 K for Cu and almost the whole temperature range for Al, which is attributed to the inelastic electron-phonon scattering. Finally, the phonon thermal conductivity in the pure metals is shown to be significantly smaller than the electron component. The current calculation scheme can quantitatively obtain the phonon-limited thermal conductivity and Lorenz ratio at intermediate/low temperatures, which is a relatively unexplored area. This approach can also be applied to other metallic systems and enables the design of high performance metallic materials.

ACKNOWLEDGMENTS

We would like to thank Dr. C. Shao, Dr. X. Gu, and Dr. W. Li for valuable discussions. This work was supported by National Natural Science Foundation of China Grant No. 51676121 (H.B.). Simulations were performed on the π 2.0 cluster supported by the Center for High Performance Computing from Shanghai Jiao Tong University.

APPENDIX A: DERIVATION OF THE EXPRESSION FOR THE TWO ELECTRON RELAXATION TIMES

Using the detailed balance condition, we have

$$S(n\mathbf{k}, m\mathbf{k}')f^0_{n\mathbf{k}}\left(1-f^0_{m\mathbf{k}'}\right) = S(m\mathbf{k}', n\mathbf{k})\left(1-f^0_{n\mathbf{k}}\right)f^0_{m\mathbf{k}'} \tag{A1}$$

with $S(n\mathbf{k}, m\mathbf{k}')$ the differential scattering rate from state $n\mathbf{k}$ to state $m\mathbf{k}'$. As we consider the electron-phonon scattering, $S(n\mathbf{k}, m\mathbf{k}')$ holds the form [36,60]

$$S(n\mathbf{k}, m\mathbf{k}') = \frac{2\pi}{\hbar}\sum_{\mathbf{q},v}|g_{mn,v}(\mathbf{k},\mathbf{q})|^2\begin{Bmatrix} n^0_{\mathbf{q}v}\delta(\varepsilon_{n\mathbf{k}}-\varepsilon_{m\mathbf{k}'}+\omega_{\mathbf{q}v}) \\ +\left[n^0_{\mathbf{q}v}+1\right]\delta(\varepsilon_{n\mathbf{k}}-\varepsilon_{m\mathbf{k}'}-\omega_{\mathbf{q}v})\end{Bmatrix}. \tag{A2}$$

We ignore the electron band indexes n and m in the next discussion for simplification. The collision term in the Eq. (1) of the main text can be expressed as

$$\left(\frac{\partial f_{\mathbf{k}}}{\partial t}\right)_{\text{coll}} = \frac{\delta f_{\mathbf{k}}}{\tau_{\mathbf{k}}} = \mathcal{I}\{f_{\mathbf{k}}\} = -\int\frac{d^3\mathbf{k}'}{(2\pi)^3}[S(\mathbf{k},\mathbf{k}')f_{\mathbf{k}}(1-f_{\mathbf{k}'}) - S(\mathbf{k}',\mathbf{k})f_{\mathbf{k}'}(1-f_{\mathbf{k}})]. \tag{A3}$$

Here $\tau_{\mathbf{k}}$ can be either $\tau_{\sigma,\mathbf{k}}$ or $\tau_{\kappa,\mathbf{k}}$. Insert $f_{\mathbf{k}} = f^0_{\mathbf{k}} + \delta f_{\mathbf{k}}$ into Eq. (A3) and we find

$$\frac{\delta f_{\mathbf{k}}}{\tau_{\mathbf{k}}} = \mathcal{I}\{f_{\mathbf{k}}\} = -\int\frac{d^3\mathbf{k}'}{(2\pi)^3}S(\mathbf{k},\mathbf{k}')\left[\delta f_{\mathbf{k}}\frac{1-f^0_{\mathbf{k}'}}{1-f^0_{\mathbf{k}}} - \delta f_{\mathbf{k}'}\frac{f^0_{\mathbf{k}}}{f^0_{\mathbf{k}'}}\right]. \tag{A4}$$

From Eq. (3), we have

$$\begin{aligned}\delta f_{\mathbf{k}} &= \tau_{\sigma,\mathbf{k}}(T)e\mathbf{v}_{\mathbf{k}}\cdot\mathrm{E}\left(\frac{\partial f^0_{\mathbf{k}}}{\partial\varepsilon_{\mathbf{k}}}\right) \quad \text{with only electrical field} \\ \delta f_{\mathbf{k}} &= \tau_{\kappa,\mathbf{k}}(T)\frac{\varepsilon(\mathbf{k})-\varepsilon_F}{T}\mathbf{v}_{\mathbf{k}}\cdot\nabla T\left(\frac{\partial f^0_{\mathbf{k}}}{\partial\varepsilon_{\mathbf{k}}}\right) \quad \text{with only temperature gradient}\end{aligned}. \tag{A5}$$

From Eq. (1), we get the following collision term for the electrical field condition:

$$\mathcal{I}\{f_{\mathbf{k}}\} = \left(-\frac{\partial f^0_{\mathbf{k}}}{\partial\varepsilon_{\mathbf{k}}}\right)\mathbf{v}_{\mathbf{k}}\cdot e\mathbf{E}. \tag{A6}$$

Similarly, for the temperature gradient condition, we have

$$\mathcal{I}\{f_{\mathbf{k}}\} = \left(-\frac{\partial f^0_{\mathbf{k}}}{\partial\varepsilon_{\mathbf{k}}}\right)\mathbf{v}_{\mathbf{k}}\cdot\frac{\varepsilon_{\mathbf{k}}-\varepsilon_F}{T}\nabla T. \tag{A7}$$

Enter the first line of Eq. (A5) and Eq. (A6) into Eq. (A4) and with the assumption $\tau_{\sigma,\mathbf{k}}v_{\mathbf{k}} \approx \tau_{\sigma,\mathbf{k}'}v_{\mathbf{k}'}$, we get

$$\frac{1}{\tau_{\sigma,\mathbf{k}}} = \int\frac{d^3\mathbf{k}'}{(2\pi)^3}\frac{1-f^0_{\mathbf{k}'}}{1-f^0_{\mathbf{k}}}\left(1-\frac{\mathbf{v}_{\mathbf{k}}\cdot\mathbf{v}_{\mathbf{k}'}}{|\mathbf{v}_{\mathbf{k}}||\mathbf{v}_{\mathbf{k}'}|}\right)S(\mathbf{k},\mathbf{k}'). \tag{A8}$$

Similarly, enter the second line of Eq. (A5) and Eq. (A7) into Eq. (A4) and with the assumption $\tau_{\kappa,\mathbf{k}}v_{\mathbf{k}} \approx \tau_{\kappa,\mathbf{k}'}v_{\mathbf{k}'}$, we get

$$\frac{1}{\tau_{\kappa,\mathbf{k}}} = \int\frac{d^3\mathbf{k}'}{(2\pi)^3}\frac{1-f^0_{\mathbf{k}'}}{1-f^0_{\mathbf{k}}}\left(1-\frac{\varepsilon_{\mathbf{k}'}-\varepsilon_F}{\varepsilon_{\mathbf{k}}-\varepsilon_F}\frac{\mathbf{v}_{\mathbf{k}}\cdot\mathbf{v}_{\mathbf{k}'}}{|\mathbf{v}_{\mathbf{k}}||\mathbf{v}_{\mathbf{k}'}|}\right)S(\mathbf{k},\mathbf{k}'). \tag{A9}$$

The term $\frac{\mathbf{v}_{\mathbf{k}}\cdot\mathbf{v}_{\mathbf{k}'}}{|\mathbf{v}_{\mathbf{k}}||\mathbf{v}_{\mathbf{k}'}|}$ in Eqs. (A8) and (A9) can also be expressed as $\cos\theta_{\mathbf{k},\mathbf{k}'}$. Change the integral Eqs. (A8) and (A9) to the summation form and insert the Eq. (A2), and we have

$$\begin{aligned}\frac{1}{\tau_{\sigma,n\mathbf{k}}} &= \frac{2\pi}{\hbar}\sum_{mv}\int_{\text{BZ}}\frac{d\mathbf{q}}{\Omega_{\text{BZ}}}|g_{mn,v}(\mathbf{k},\mathbf{q})|^2\frac{1-f^0_{m\mathbf{k}'}(T)}{1-f^0_{n\mathbf{k}}(T)}\begin{Bmatrix} n^0_{\mathbf{q}v}(T)\delta(\varepsilon_{n\mathbf{k}}-\varepsilon_{m\mathbf{k}'}+\omega_{\mathbf{q}v}) \\ +\left[n^0_{\mathbf{q}v}(T)+1\right]\delta(\varepsilon_{n\mathbf{k}}-\varepsilon_{m\mathbf{k}'}-\omega_{\mathbf{q}v})\end{Bmatrix}(1-\cos\theta_{n\mathbf{k},m\mathbf{k}'}) \\ \frac{1}{\tau_{\kappa,n\mathbf{k}}} &= \frac{2\pi}{\hbar}\sum_{mv}\int_{\text{BZ}}\frac{d\mathbf{q}}{\Omega_{\text{BZ}}}|g_{mn,v}(\mathbf{k},\mathbf{q})|^2\frac{1-f^0_{m\mathbf{k}'}(T)}{1-f^0_{n\mathbf{k}}(T)}\begin{Bmatrix} n^0_{\mathbf{q}v}(T)\delta(\varepsilon_{n\mathbf{k}}-\varepsilon_{m\mathbf{k}'}+\omega_{\mathbf{q}v}) \\ +\left[n^0_{\mathbf{q}v}(T)+1\right]\delta(\varepsilon_{n\mathbf{k}}-\varepsilon_{m\mathbf{k}'}-\omega_{\mathbf{q}v})\end{Bmatrix}\left(1-\frac{\varepsilon_{m\mathbf{k}'}-\varepsilon_F}{\varepsilon_{n\mathbf{k}}-\varepsilon_F}\cos\theta_{n\mathbf{k},m\mathbf{k}'}\right).\end{aligned} \tag{A10}$$

We add the electron band indexes n and m in Eq. (A10). The term $\frac{\varepsilon_{m\mathbf{k}'}-\varepsilon_F}{\varepsilon_{n\mathbf{k}}-\varepsilon_F}\cos\theta_{n\mathbf{k},m\mathbf{k}'}$ in the second line of Eq. (A10) can be further dismissed [4,34]. Therefore, we obtain the final expression for the two electron scattering rates:

$$\frac{1}{\tau_{\sigma,n\mathbf{k}}}=\frac{2\pi}{\hbar}\sum_{mv}\int_{\mathrm{BZ}}\frac{d\mathbf{q}}{\Omega_{\mathrm{BZ}}}|g_{mn,v}(\mathbf{k},\mathbf{q})|^2\frac{1-f^0_{m\mathbf{k}'}(T)}{1-f^0_{n\mathbf{k}}(T)}\begin{Bmatrix}n^0_{\mathbf{q}v}(T)\delta(\varepsilon_{n\mathbf{k}}-\varepsilon_{m\mathbf{k}'}+\omega_{\mathbf{q}v})\\+\left[n^0_{\mathbf{q}v}(T)+1\right]\delta(\varepsilon_{n\mathbf{k}}-\varepsilon_{m\mathbf{k}'}-\omega_{\mathbf{q}v})\end{Bmatrix}(1-\cos\theta_{n\mathbf{k},m\mathbf{k}'})$$

$$\frac{1}{\tau_{\kappa,n\mathbf{k}}}=\frac{2\pi}{\hbar}\sum_{mv}\int_{\mathrm{BZ}}\frac{d\mathbf{q}}{\Omega_{\mathrm{BZ}}}|g_{mn,v}(\mathbf{k},\mathbf{q})|^2\frac{1-f^0_{m\mathbf{k}'}(T)}{1-f^0_{n\mathbf{k}}(T)}\begin{Bmatrix}n^0_{\mathbf{q}v}(T)\delta(\varepsilon_{n\mathbf{k}}-\varepsilon_{m\mathbf{k}'}+\omega_{\mathbf{q}v})\\+\left[n^0_{\mathbf{q}v}(T)+1\right]\delta(\varepsilon_{n\mathbf{k}}-\varepsilon_{m\mathbf{k}'}-\omega_{\mathbf{q}v})\end{Bmatrix}. \tag{A11}$$

From Eq. (A11), it can be seen that there exists an efficiency factor in momentum relaxation time, while there is no efficiency factor in energy relaxation time. In our main text, we use the following expressions for the two electron relaxation times,

$$\frac{1}{\tau_{\sigma,n\mathbf{k}}}=\frac{2\pi}{\hbar}\sum_{mv}\int_{\mathrm{BZ}}\frac{d\mathbf{q}}{\Omega_{\mathrm{BZ}}}|g_{mn,v}(\mathbf{k},\mathbf{q})|^2\begin{Bmatrix}\left[n^0_{\mathbf{q}v}(T)+f^0_{m\mathbf{k}'}(T)\right]\delta(\varepsilon_{n\mathbf{k}}-\varepsilon_{m\mathbf{k}'}+\omega_{\mathbf{q}v})\\+\left[n^0_{\mathbf{q}v}(T)+1-f^0_{m\mathbf{k}'}(T)\right]\delta(\varepsilon_{n\mathbf{k}}-\varepsilon_{m\mathbf{k}'}-\omega_{\mathbf{q}v})\end{Bmatrix}(1-\cos\theta_{n\mathbf{k},m\mathbf{k}'})$$

$$\frac{1}{\tau_{\kappa,n\mathbf{k}}}=\frac{2\pi}{\hbar}\sum_{mv}\int_{\mathrm{BZ}}\frac{d\mathbf{q}}{\Omega_{\mathrm{BZ}}}|g_{mn,v}(\mathbf{k},\mathbf{q})|^2\begin{Bmatrix}\left[n^0_{\mathbf{q}v}(T)+f^0_{m\mathbf{k}'}(T)\right]\delta(\varepsilon_{n\mathbf{k}}-\varepsilon_{m\mathbf{k}'}+\omega_{\mathbf{q}v})\\+\left[n^0_{\mathbf{q}v}(T)+1-f^0_{m\mathbf{k}'}(T)\right]\delta(\varepsilon_{n\mathbf{k}}-\varepsilon_{m\mathbf{k}'}-\omega_{\mathbf{q}v})\end{Bmatrix}. \tag{A12}$$

There are some differences between Eqs. (A11) and (A12). It is claimed in Ref. [35] that the two expressions are equal. The relaxation times in Eq. (A11) are also called transport relaxation times [35]. The scattering rates calculated by Eqs. (A11) and (A12) are shown in Fig. 12. Both momentum relaxation times and energy relaxation times predicted by Eqs. (A11) and (A12) are almost the same.

APPENDIX B: ALLEN'S MODEL FOR TRANSPORT COEFFICIENTS

The electrical resistivity is given by [18,51]

$$\rho_{el}(T)=\frac{1}{\sigma(T)}=\frac{2\pi V k_B T}{e^2\hbar N_F\langle v_\alpha^2\rangle}\int_0^\infty\frac{d\omega}{\omega}\frac{x^2}{\sinh^2 x}\alpha^2F_{tr}(\omega). \tag{B1}$$

N_F is the electron density of state per spin and per unit cell at the Fermi surface. α is the coordinate of the Cartesian system. $\langle v_\alpha^2\rangle$ means the average velocity square in coordinate α. $x=\hbar\omega/2k_BT$ is a dimensionless parameter. The Eliashberg transport function $\alpha^2F_{tr}$is expressed as [30]

$$\alpha^2F_{tr}(\omega)=\frac{1}{N(\varepsilon_F)}\sum_{\mathbf{q},v}\sum_{\mathbf{k}nm}|g_{mn,v}(\mathbf{k},\mathbf{q})|^2\delta(\hbar\omega-\hbar\omega_{\mathbf{q}v})\times\delta(\varepsilon_{\mathbf{k}n}-\varepsilon_F)\delta(\varepsilon_{\mathbf{k}+\mathbf{q}m}-\varepsilon_F)\alpha_{\mathbf{k}+\mathbf{q}m,\mathbf{k}n}, \tag{B2}$$

where $\alpha_{\mathbf{k}+\mathbf{q}m,\mathbf{k}n}$ is the efficiency factor in Eq. (6).

The thermal resistivity is given by [18,51]

$$\begin{aligned}\rho_{th}(T)&=\frac{1}{\kappa_{\mathrm{el}}(T)}=\frac{1}{L_0T}\frac{2\pi Vk_BT}{e^2\hbar N_F\langle v_\alpha^2\rangle}\int_0^\infty\frac{d\omega}{\omega}\frac{x^2}{\sinh^2x}\left\{\left[1-\frac{2}{\pi^2}x^2\right]\alpha^2F_{tr}(\omega)+\frac{6}{\pi^2}x^2\alpha^2F(\omega)\right\}\\&=\frac{1}{L_0}\frac{2\pi Vk_B}{e^2\hbar N_F\langle v_\alpha^2\rangle}\begin{Bmatrix}\int_0^\infty\frac{d\omega}{\omega}\frac{x^2}{\sinh^2x}\alpha^2F_{tr}(\omega)\\+\int_0^\infty\frac{d\omega}{\omega}\frac{x^2}{\sinh^2x}\left\{\frac{2}{\pi^2}x^2\alpha^2F_{tr}(\omega)+\frac{6}{\pi^2}x^2\alpha^2F(\omega)\right\}\end{Bmatrix}\\&=\frac{1}{L_0}\frac{2\pi Vk_B}{e^2\hbar N_F\langle v_\alpha^2\rangle}\{\mathcal{I}_1+\mathcal{I}_2\}\end{aligned} \tag{B3}$$

with $\mathcal{I}_1=\int_0^\infty\frac{d\omega}{\omega}\frac{x^2}{\sinh^2x}\alpha^2F_{tr}(\omega)$ and $\mathcal{I}_2=\int_0^\infty\frac{d\omega}{\omega}\frac{x^2}{\sinh^2x}\{\frac{2}{\pi^2}x^2\alpha^2F_{tr}(\omega)+\frac{6}{\pi^2}x^2\alpha^2F(\omega)\}$.

The Wiedemann-Franz law holds as we ignore $\mathcal{I}_2$ in Eq. (B3). α^2F is the Eliashberg spectral function, which is read as [30]

$$\alpha^2F(\omega)=\frac{1}{N(\varepsilon_F)}\sum_{\mathbf{q},v}\sum_{\mathbf{k}nm}|g_{mn,v}(\mathbf{k},\mathbf{q})|^2\delta(\hbar\omega-\hbar\omega_{\mathbf{q}j})\times\delta(\varepsilon_{\mathbf{k}n}-\varepsilon_F)\delta(\varepsilon_{\mathbf{k}+\mathbf{q}m}-\varepsilon_F). \tag{B4}$$

APPENDIX C: LORENZ RATIO BY BG MODEL

The Bloch-Grüneisen model gives the Lorenz ratio as

$$L=\frac{L_0}{1+\frac{3}{\pi^2}\left(\frac{k_F}{q_D}\right)^2\left(\frac{\theta_D}{T}\right)^2-\frac{1}{2\pi^2}\frac{J_7(\theta/T)}{J_5(\theta/T)}}, \tag{C1}$$

where k_F and q_D are the Fermi wave vector and Debye wave vector, respectively. θ_D is the Debye temperature, which is predicted as 322 K for Cu and 446 K for Al from first principles. J_n (n is an integer) is defined as

$$J_n\left(\frac{\theta}{T}\right)\equiv\int_0^{\theta/T}\frac{x^ne^x}{(e^x-1)^2}dx. \tag{C2}$$

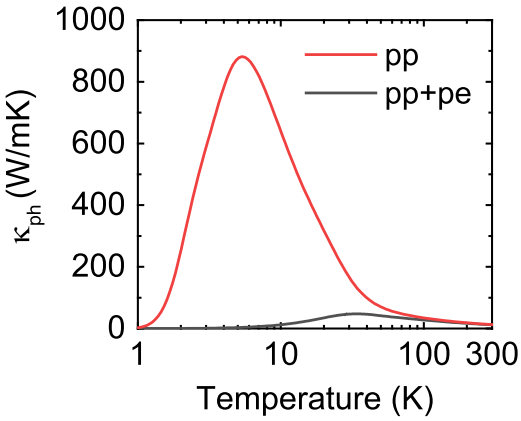

FIG. 13. The phonon thermal conductivity without (pp) and with ($pp + pe$) phonon-electron scattering for Cu.

APPENDIX D: PHONON-ELECTRON SCATTERING EFFECTS ON PHONON THERMAL CONDUCTIVITY

The phonon thermal conductivity is given by

$$\kappa_{\mathrm{ph},\alpha\beta} = \sum_{\lambda} c_{v,\lambda} v_{\lambda,\alpha} v_{\lambda,\beta} \tau_{\lambda}, \tag{D1}$$

where λ is the phonon mode denotation. $c_{v,\lambda}$ is the phonon heat capacity, v_{λ} is the phonon group velocity, and τ_{λ} is the phonon relaxation time. All three parameters are phonon mode dependent. According to Matthiessen's rule, the phonon relaxation time can be expressed as $1/\tau_{\lambda} = 1/\tau_{\lambda}^{PPI} + 1/\tau_{\lambda}^{PEI}$. Here, $1/\tau_{\lambda}^{PPI}$ and $1/\tau_{\lambda}^{PEI}$ are the phonon-scattering rates induced by phonon-phonon and phonon-electron scattering.

To demonstrate the effects of phonon-electron scattering, the phonon thermal conductivity without and with phonon-electron scattering for Cu is shown in Fig. 13.

[1] H. Bao, J. Chen, X. Gu, and B. Cao, ES Energy Environ. **1**, 16 (2018).
[2] D. G. Cahill, P. V. Braun, G. Chen, D. R. Clarke, S. Fan, K. E. Goodson, P. Keblinski, W. P. King, G. D. Mahan, A. Majumdar *et al.*, Appl. Phys. Rev. **1**, 011305 (2014).
[3] L. Lorenz, Ann. Phys. (Berlin, Ger.) **249**, 422 (1881).
[4] A. Lavasani, D. Bulmash, and S. Das Sarma, Phys. Rev. B **99**, 085104 (2019).
[5] T. M. Tritt, *Thermal Conductivity: Theory, Properties, and Applications* (Springer Science & Business Media, New York, 2005).
[6] Y. S. Touloukian, R. W. Powell, C. V. Ha, and P. G. Klemens, *Thermophysical Properties of Matter - The TPRC Data Series. Vol. 1. Thermal Conductivity - Metallic Elements and Alloys* (IFI/Plenum, New York, 1970).
[7] G. White and R. Tainsh, Phys. Rev. **119**, 1869 (1960).
[8] M. Yao, M. Zebarjadi, and C. P. Opeil, J. Appl. Phys. **122**, 135111 (2017).
[9] H. N. D. Lang, H. v. Kempen, and P. Wyder, J. Phys. F: Met. Phys. **8**, L39 (1978).
[10] W. H. Butler and R. K. Williams, Phys. Rev. B **18**, 6483 (1978).
[11] R. L. Powell, W. J. Hall, and H. M. Roder, J. Appl. Phys. **31**, 496 (1960).
[12] F. Bloch, Z. Phys. **52**, 555 (1929).
[13] E. Grüneisen, Ann. Phys. (Berlin, Ger.) **408**, 530 (1933).
[14] Q. Zheng, A. B. Mei, M. Tuteja, D. G. Sangiovanni, L. Hultman, I. Petrov, J. E. Greene, and D. G. Cahill, Phys. Rev. Mater. **1**, 065002 (2017).
[15] G. K. Madsen and D. J. Singh, Comput. Phys. Commun. **175**, 67 (2006).
[16] J. I. Mustafa, M. Bernardi, J. B. Neaton, and S. G. Louie, Phys. Rev. B **94**, 155105 (2016).
[17] B. Xu and M. J. Verstraete, Phys. Rev. Lett. **112**, 196603 (2014).
[18] P. Allen, Phys. Rev. B **17**, 3725 (1978).
[19] S. Y. Savrasov and D. Y. Savrasov, Phys. Rev. B **54**, 16487 (1996).
[20] R. Bauer, A. Schmid, P. Pavone, and D. Strauch, Phys. Rev. B **57**, 11276 (1998).
[21] N. Marzari, A. A. Mostofi, J. R. Yates, I. Souza, and D. Vanderbilt, Rev. Mod. Phys. **84**, 1419 (2012).
[22] A. Jain and A. J. H. McGaughey, Phys. Rev. B **93**, 081206(R) (2016).
[23] Z. Tong, S. Li, X. Ruan, and H. Bao, Phys. Rev. B **100**, 144306 (2019).
[24] Y. Chen, J. Ma, and W. Li, Phys. Rev. B **99**, 020305(R) (2019).
[25] Z. Tong and H. Bao, Int. J. Heat Mass Transfer **117**, 972 (2018).
[26] S. Li, Z. Tong, and H. Bao, J. Appl. Phys. **126**, 025111 (2019).
[27] B. Liao, J. Zhou, B. Qiu, M. S. Dresselhaus, and G. Chen, Phys. Rev. B **91**, 235419 (2015).
[28] T.-H. Liu, J. Zhou, M. Li, Z. Ding, Q. Song, B. Liao, L. Fu, and G. Chen, Proc. Natl. Acad. Sci. U.S.A. **115**, 879 (2018).
[29] X. Gu, S. Li, and H. Bao, Int. J. Heat Mass Transfer **160**, 120165 (2020).
[30] S. Poncé, E. R. Margine, C. Verdi, and F. Giustino, Comput. Phys. Commun. **209**, 116 (2016).
[31] Z. Stanojević, O. Baumgartner, M. Karner, L. Filipović, C. Kernstock, and H. Kosina, in *2014 International Conference on Simulation of Semiconductor Processes and Devices (SISPAD)* (IEEE, New York, 2014), pp. 181–184.
[32] U. Mizutani, *Introduction to the Electron Theory of Metals* (Cambridge University Press, Cambridge, UK, 2001).
[33] J. M. Ziman, *Electrons and Phonons: The Theory of Transport Phenomena in Solids* (Oxford University Press, Oxford, UK, 2001).
[34] T. Sohier, D. Campi, N. Marzari, and M. Gibertini, Phys. Rev. Mater. **2**, 114010 (2018).
[35] T. Gunst, T. Markussen, K. Stokbro, and M. Brandbyge, Phys. Rev. B **93**, 035414 (2016).
[36] G. D. Mahan, *Many-particle Physics* (Springer Science & Business Media, New York, 2013).
[37] D. Fan, H. Liu, L. Cheng, J. Liang, and P. Jiang, J. Mater. Chem. A **6**, 12125 (2018).
[38] P. Giannozzi, S. Baroni, N. Bonini, M. Calandra, R. Car, C. Cavazzoni, D. Ceresoli, G. L. Chiarotti, M. Cococcioni, I. Dabo *et al.*, J. Phys.: Condens. Matter **21**, 395502 (2009).
[39] J. P. Perdew, K. Burke, and M. Ernzerhof, Phys. Rev. Lett. **77**, 3865 (1996).
[40] C. G. Broyden, IMA J. Appl. Math. **6**, 76 (1970).
[41] R. Fletcher, Comput. J. **13**, 317 (1970).
[42] D. Goldfarb, Math. Comput. **24**, 23 (1970).

[43] D. F. Shanno, Math. Comput. **24**, 647 (1970).
[44] P. Eckerlin, K. H. Hellwege, H. Kandler, and A. M. Hellwege, *Structure Data of Elements and Intermetallic Phases* (Springer, Berlin, 1971).
[45] S. Baroni, S. de Gironcoli, A. Dal Corso, and P. Giannozzi, Rev. Mod. Phys. **73**, 515 (2001).
[46] See Supplemental Material at http://link.aps.org/supplemental/10.1103/PhysRevB.102.174306 for details on (i) phonon dispersions and electron band structures for Cu and Al, (ii) convergence test on the broadening parameter of Al at 100 and 300 K, (iii) convergence test on the Fermi window width, (iv) electrical transport properties of Nb and Ta.
[47] R. t. Stedman and G. Nilsson, Phys. Rev. **145**, 492 (1966).
[48] R. Nicklow, G. Gilat, H. Smith, L. Raubenheimer, and M. Wilkinson, Phys. Rev. **164**, 922 (1967).
[49] W. Li, J. Carrete, N. A. Katcho, and N. Mingo, Comput. Phys. Commun. **185**, 1747 (2014).
[50] F. Rittweger, N. F. Hinsche, and I. Mertig, J. Phys.: Condens. Matter **29**, 355501 (2017).
[51] F. J. Pinski, P. B. Allen, and W. H. Butler, Phys. Rev. B **23**, 5080 (1981).
[52] J. Bass, in *Electrical Resistivity, Kondo and Spin Fluctuation Systems, Spin Glasses and Thermopower*, Landolt-Börnstein Numerical Data and Functional Relationships in Science and Technology, Vol. 15, New Series, Group III: Crystal and Solid State Physics, edited by K.-H. Hellwege and J. L. Olsen (Springer Verlag, Berlin, 1983).
[53] N. T. Hung, A. R. Nugraha, and R. Saito, Appl. Phys. Lett. **111**, 092107 (2017).
[54] W. Li, Phys. Rev. B **92**, 075405 (2015).
[55] A. Giri, J. T. Gaskins, L. Li, Y.-S. Wang, O. V. Prezhdo, and P. E. Hopkins, Phys. Rev. B **99**, 165139 (2019).
[56] A. Giri, M. V. Tokina, O. V. Prezhdo, and P. E. Hopkins, Mater. Today Phys. **12**, 100175 (2020).
[57] J. Coulter, R. Sundararaman, and P. Narang, Phys. Rev. B **98**, 115130 (2018).
[58] M. Kawamura, Comput. Phys. Commun. **239**, 197 (2019).
[59] Y. Wang, Z. Lu, and X. Ruan, J. Appl. Phys. **119**, 225109 (2016).
[60] M. Lundstrom, *Fundamentals of Carrier Transport* (Cambridge University Press, Cambridge, UK, 2009).